Characterization of hybrid quantum eigenstates in systems with mixed classical phase space

Anant Vijay Varma [1,*] Amichay Vardi [1,2,†] and Doron Cohen [3,‡]
[1]*Department of Chemistry, Ben-Gurion University of the Negev, Beer Sheva 84105, Israel*
[2]*ITAMP, Harvard-Smithsonian Center for Astrophysics, Cambridge, Massachusetts 02138, USA*
[3]*Department of Physics, Ben-Gurion University of the Negev, Beer Sheva 84105, Israel*

(Received 10 March 2024; accepted 20 May 2024; published 10 June 2024)

Generic low-dimensional Hamiltonian systems feature a structured, mixed classical phase space. The traditional Percival classification of quantum spectra into regular states supported by quasi-integrable regions and irregular states supported by quasichaotic regions turns out to be insufficient to capture the richness of the Hilbert space. Berry's conjecture and the eigenstate thermalization hypothesis are not applicable and quantum effects such as tunneling, scarring, and localization do not obey the standard paradigms. We demonstrate these statements for a prototype Bose-Hubbard model. We highlight the hybridization of chaotic and regular regions from opposing perspectives of ergodicity and localization.

DOI: 10.1103/PhysRevE.109.064207

I. INTRODUCTION

In a seminal paper, Percival suggested a classification of quantum mechanical spectra into regular and irregular eigenstates [1], supported, respectively, by quasiregular islands and chaotic seas within the classical phase space [2]. Whereas regular states are restricted to invariant tori, irregular states are ergodic in the chaotic sea in consistency with Random Matrix Theory (RMT) predictions [3]. For large systems, this implies a thermal expectation value for local observables, an observation known as the eigenstate thermalization hypothesis (ETH) [4–7]. The binary classification of quantum eigenstates is a widely accepted paradigm in studies of quantum chaos.

In reality, the picture is more complicated. A sharp distinction between regular and chaotic states is not generally practical, and spectral analysis is not sufficiently revealing [8]. In this paper, we consider a prototype mixed-phase-space system. We find that the statistical properties of chaotic eigenstates that dwell in phase space with mixed regular and chaotic motion are substantially different from those of eigenstates supported by a globally connected chaotic sea. We also identify special nonergodic states that are dynamically localized [9–11] in chaotic regions. The existence of the latter is related to slow dynamics near unstable stationary points (SPs) and can be viewed as an extreme type of scarring [12–15].

Our paper demonstrates that quantization of the mixed classical phase space is a double-edged sword. On the one hand, quantum tunneling can connect classically separated chaotic and regular regions, resulting in hybrid quantum eigenstates that do not adhere to the standard classification. On the other hand, there is also an opposite effect due to dynamical localization there are states that are not fully ergodic despite the prevailing chaos. The underlying mechanism of this localization is the slow dynamics in the vicinity of an unstable hyperbolic point embedded in chaos. As such, it is different from previous studies of dynamical localization in the peripheral regions of the chaotic sea [16,17] and from localization by remnants of Kolmogorov-Arnold-Moser (KAM) tori [18–20].

II. BOSE-HUBBARD TRIMER HAMILTONIAN

The Bose-Hubbard (BH) model, see Ref. [21] and references within, is a paradigm for quantum chaos studies. Of particular interest is the three-site (trimer) model, whose mixed phase-space is of interest, e.g., in the context of superflow stability [22] and phase separation [23]. The Hamiltonian for N Bosons is written in terms of three second-quantized modes:

$$H = V\hat{n}_2 + \frac{U}{2}\sum_{i=1}^{3}\hat{n}_i^2 - \frac{\Omega}{2}\left(\hat{a}_2^\dagger\hat{a}_1 + \hat{a}_3^\dagger\hat{a}_2 + \text{H.c.}\right), \qquad (1)$$

where $\hat{a}_i^\dagger$ and $\hat{a}_i$ are Bosonic creation and annihilation operators in the ith local mode. U is the interaction strength, Ω is the hopping parameter, and V is the middle site bias. The dimensionless parameters of the model are

$$u = \frac{NU}{\Omega}, \qquad v = \frac{V}{\Omega}. \qquad (2)$$

Throughout the paper, we use units of time such that $\Omega = 1$ and set $v = 0.1$.

In the classical limit, the field operators $\hat{a}_i$ can be replaced by complex numbers $a_i = \sqrt{n_i}e^{i\phi_i}$. Thus, the classical motion has three degrees of freedom, with $\{n_i, \phi_i\}$, $i = 1, 2, 3$ serving as conjugate action-angle variables. Owing to the U(1) symmetry, the classical phase space can be further reduced to two degrees of freedom. Throughout this paper, our choice of canonical variables is $p_1 = n_1/N$, $p_2 = n_2/N$, $q_1 = \phi_1 - \phi_3$,

*Contact author: varma@post.bgu.ac.il
†Contact author: avardi@bgu.ac.il
‡Contact author: dcohen@bgu.ac.il

and $q_2 = \phi_2 - \phi_3$, resulting in the classical Hamiltonian:

$$\frac{H_{\rm cl}}{N} = V\ p_2 + \frac{NU}{2}\left(p_1^2 + p_2^2 + (1-p_1-p_2)^2\right) - \Omega(\sqrt{p_1 p_2}\cos(q_1-q_2) + \sqrt{p_2(1-p_1-p_2)}\cos q_2). \tag{3}$$

The quantum Hilbert space of the N-particle system is spanned by the Fock basis $|\mathbf{n}\rangle = |n_1, n_2\rangle$, with $n_3 = N - n_1 - n_2$. Its dimension is thus

$$\mathcal{N} \ = \ \tfrac{1}{2}(N+1)(N+2)\,. \tag{4}$$

III. EIGENSTATE CHARACTERIZATION

Diagonalizing H in the Fock basis, we obtain the quantum spectrum $H|E_\nu\rangle = E_\nu|E_\nu\rangle$. The purity of each eigenstate $|E_\nu\rangle$ is $S = \mathrm{Tr}[(\rho^{(\rm sp)})^2]$, where

$$\rho^{(\rm sp)} = (1/N)(\langle a_i^\dagger a_j\rangle)_{i,j=1,2,3} \tag{5}$$

is the one-particle probability matrix. Eigenstates may be visualized via their Husimi phase-space distribution,

$$Q_\nu(\alpha) = |\langle\alpha|E_\nu\rangle|^2, \tag{6}$$

where $|\alpha\rangle$ are coherent states localized at $\alpha = (q_1, q_2, p_1, p_2)$. Alternatively, the eigenstates can be represented by their Fock-space distribution:

$$X_{\nu,n} = |\langle\mathbf{n}|E_\nu\rangle|^2\,. \tag{7}$$

To characterize this distribution for the various eigenstates, we calculate the following measures:

$$R_q = \sum_{n=1}^{\mathcal{N}} X_{\nu,n}^q, \tag{8}$$

$$M_q = R_q^{-\frac{1}{q-1}}. \tag{9}$$

The quantities R_2 and M_2 are, respectively, the inverse participation ratio (IPR) and the participation number (PN) in the Fock (computational) basis. Higher $q > 2$ moments provide more information on the shape of the Fock space distribution. In the limit $q \to 1$, one obtains $M_1 = \exp(\tilde{R}_1)$, with $\tilde{R}_1 = -\sum_{n=1}^{\mathcal{N}} X_{\nu,n} \ln X_{\nu,n}$, aka Shanon's entropy.

Averaging over all eigenstates within a narrow energy window around E, we define the mean intensities X_n. The effective dimension of this energy shell is thus

$$\mathcal{N}_{\rm eff} = \left[\sum_n |X_n|^2\right]^{-1}. \tag{10}$$

Rescaling the intensities as

$$x_{\nu,n} = \mathcal{N}_{\rm eff} X_{\nu,n} \tag{11}$$

ensures that their average is roughly unity. For GOE chaotic states, we expect Porter-Thomas intensity statistics [24,25],

$$P(x) = \frac{1}{\sqrt{x}} e^{-x/2}\,, \tag{12}$$

resulting in

$$M_q^{\rm GOE} = \left[\frac{2^q}{\sqrt{\pi}}\Gamma(q+1/2)\right]^{-\frac{1}{q-1}} \mathcal{N}_{\rm eff}. \tag{13}$$

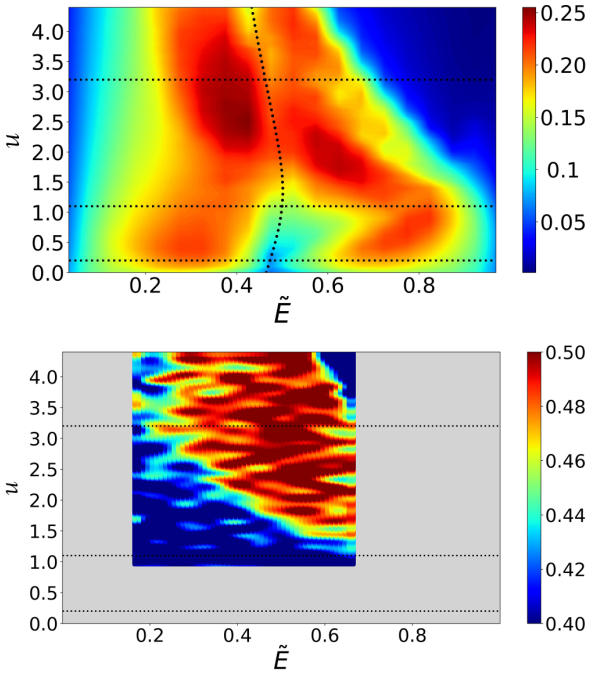

FIG. 1. Parametric evolution of the trimer spectrum. Upper panel: Mean participation. The trimer spectrum at each given value of u is distributed into 100 equal-width energy bins and the participation ratio $M_2/\mathcal{N}$ is averaged over all eigenstates in each bin. High participation ratios indicate chaos. The total number of particles is $N = 150$ and the detuning is $v = 0.1$. The black dotted line marks the energy $\tilde{E}_{\rm SP}$, while the horizontal dotted lines indicate (in order of increasing u) the loss of dynamical stability, the onset of chaos, and the restoration of integrability as discussed in Sec. V. Lower panel: The r level-spacing statistics. Each bin is color-coded by the the average r value. Regions of bad statistics are grey. GOE statistics ($r \approx 0.53$) indicates underlying chaos.

It is easily verified that for $q = 2$ one obtains the well-known participation number $\mathrm{PN}_{\rm GOE} = \mathcal{N}/3$. For $q = 10$, the expected Fock-basis moment for a chaotic eigenstate is $M_{10}^{\rm GOE} = \mathcal{N}/9.54$.

IV. MAPPING THE TRIMER SPECTRUM

This section provides a global view of the Bose-Hubbard trimer's spectrum. Rescaling the eigenenergies as $\tilde{E}_\nu = (E_\nu - E_{\rm min})/(E_{\rm max} - E_{\rm min}) \in [0, 1]$, we plot in Fig. 1 the mean Fock participation number M_2 of energy eigenstates lying within energy bins around $\tilde{E}$ at different values of the interaction parameter u. The spectrum evolves parameterically in a nontrivial way, with large PN that indicates underlying chaos observed around $u \sim 3$. Subsequent analysis focuses on this regime. In the lower panel of Fig. 1, we show the level statistics. The definition of the spacing ratio r around E_ν, and details on the statistical analysis, are provided in Appendix B of Ref. [17]. An average value $r \approx 0.53$ that is based on the Gaussian orthogonal ensemble (GOE), as opposed to the Poissonian $r \approx 0.386$, is commonly regarded as an indication for underlying chaos. While the r measure better identifies

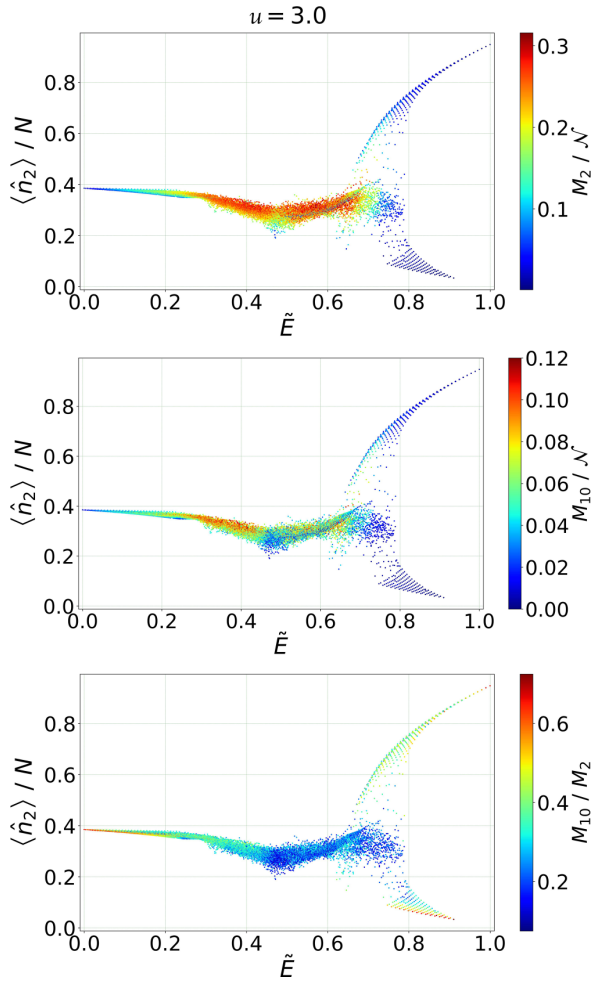

FIG. 2. Tomography of the spectrum. Detailed view of the trimer spectrum at $u = 3$. Each point corresponds to one many-body eigenstate, classified according to its rescaled energy $\tilde{E}_v$ and central site occupation $\langle \hat{n}_2 \rangle / N$, and color-coded according to $M_2/\mathcal{N}$ (top panel), $M_{10}/\mathcal{N}$ (middle panel), and M_{10}/M_2 (bottom panel). Parameters are the same as in Fig. 1.

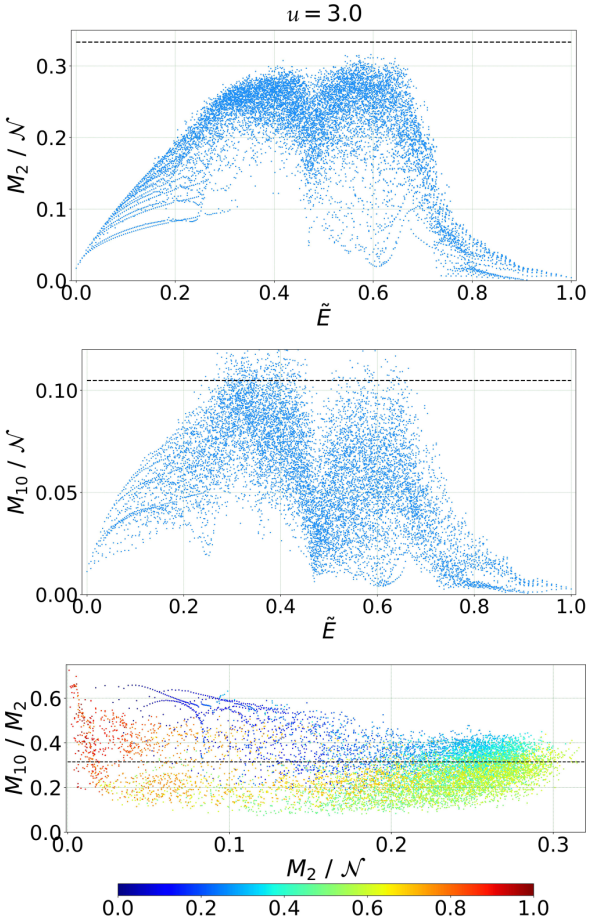

FIG. 3. Moments of the Fock space distribution of the eigenstates. Scatter plots of the data displayed in Fig. 2: (a) $M_2/\mathcal{N}$ vs $\tilde{E}$; (b) $M_{10}/\mathcal{N}$ vs $\tilde{E}$; (3) M_{10}/M_2 vs $M_2/\mathcal{N}$, color coded with $\tilde{E}$. Horizontal dashed lines mark the expected values according to Eq. (13) for GOE ergodic states.

this chaos, the M_q measure, that can be large also for quasi-integrable states, is more sensitive to variations in quantum ergodicity.

A detailed view of the spectrum for $u = 3.0$ is provided in Fig. 2. Each point represents an eigenstate of the Hamiltonian Eq. (1). Due to mirror symmetry, specification of the middle site's normalized population $\langle \hat{n}_2 \rangle / N$ is sufficient to determine the population in the other sites. In the absence of bias and interactions $u = v = 0$, the system's eigenstates would be orbital-Fock states, i.e., symmetrized direct products of one-particle orbitals. In this case, the spectrum would be degenerate in n_2, because moving pairs of particles from the dark state orbital $(|1\rangle - |3\rangle)/\sqrt{2}$ into the other two orbitals does not change the energy. Introducing a small bias $v \neq 0$, the spectrum of Fig. 2 is stretched in the vertical direction, making it easier to understand its structure. The introduction of finite interaction ($u \neq 0$) further deforms the displayed spectrum. The value $u = 3$ is chosen because chaotic regions in the classical phase space are relatively large.

The color maps in the three panels of Fig. 2 display information on the normalized participation number $M_2/\mathcal{N}$, the shape-sensitive moment $M_{10}/\mathcal{N}$, and the ratio between them M_{10}/M_2. The same information is displayed in Fig. 3. The low-energy range of the spectrum exhibits small PNs. The same applies in the high-energy range, where the interaction induces self-trapping either in the middle or in the outer sites. Chaos prevails at intermediate energies in the range $0.3 < \tilde{E} < 0.7$.

Interestingly, the ergodicity measures exhibit nontrivial dependence on E. Both M_2 and M_{10} roughly agree with the GOE prediction throughout the chaotic energy range, but show a pronounced narrow dip at the energy $E = E_{\mathrm{SP}}$. This is the energy of an underlying SP that supports the dark state, see further discussion in the following section. Its energy for

different values of u is indicated by the black dotted line in Fig. 1.

More importantly, the E dependence of the M_{10}/M_2 ratio reveals information that eludes the M_2 measure alone. The ratio is significantly lower in the $E > E_{\rm SP}$ range compared with the $E < E_{\rm SP}$ range. As shown in Sec. VI, this drop reflects an underlying classical transition from *hard chaos*, where the motion on the pertinent energy surface is fully chaotic, to *mixed chaos*, where the energy surface contains quasi-integrable regions of non-negligible measure.

V. THE CENTRAL STATIONARY POINT

The classical Hamiltonian has a midspectrum SP at $\alpha_{\rm SP} = (1/\sqrt{2}, 0, -1/\sqrt{2})$, that corresponds to the dark-state orbital. The corresponding canonical variables are thus $p_1 = 1/2$, $q_1 = \pi$, $p_2 = 0$, while q_2 is ill defined. This SP dominates the phase-space structure. Its energy is

$$E_{\rm SP} = \tfrac{1}{4}{\rm Nu}. \tag{14}$$

Quantum mechanically the SP supports a coherent state where all particles occupy the dark state orbital, namely,

$$|\alpha_{\rm SP}\rangle = \frac{1}{\sqrt{2^N N!}}(\hat{a}_1^\dagger - \hat{a}_3^\dagger)^N\,|0\rangle\ . \tag{15}$$

The midspectrum SP remains a stationary point of the classical dynamics even in the presence of interaction. It is a fixed point of the discrete nonlinear Schrödinger equation [26,27]. By contrast, the SP-supported coherent state is an exact eigenstate of the many-body Hamiltonian only for $u = 0$. Calculating the overlap $Q_v(\alpha_{\rm SP})$ for all the many-body eigenstates $|E_v\rangle$, we define an SP-supported eigenstate as the one having the maximal overlap. We aim to relate the properties of this many-body eigenstate to the classical stability of the underlying SP.

The classical stability analysis of the midspectrum SP is presented in Appendix. There are three degrees of freedom and hence three Bogoliubov frequencies. One of them must be $\omega_0 = 0$ due to the conservation of the number of particles. The two other frequencies are real up to the lower instability threshold $u = 2v$ where they become complex. Then, for large enough u, stability is regained due to self-trapping. For $v = 0$, this upper stability threshold lies at $u = \sqrt{8}$, whereas for $v = 0.1$ it is $u = 3.2$. The dependence of the Boguliobov frequencies on u is displayed in Fig. 4. It should be noted that while the emergence of complex frequencies in between these thresholds indicates the loss of dynamical stability of the SP, it does not provide a way to identify the emergence of chaos in the vicinity of the SP.

In Fig. 5, we plot, as a function of u, the purity S, the overlap $Q(\alpha_{\rm SP})$, and the participation number M_2 of the SP-supported eigenstate. The classical instability is clearly reflected in the low coherence measures and in the high participation number. However, within this range of instability, a transition takes place at $u = 1.1$. In what follows, we show that this transition can be attributed to the emergence of chaos in the vicinity of the unstable SP.

The top panels of Fig. 6 show the $p_2 = 1/2$ Poincare sections at $E_{\rm SP}$ throughout the u parameter range. In the quasilinear regime ($u = 0.1$, left column), it is clear that the representative trajectory is supported by a KAM torus [28,29]. For larger interaction strengths ($u = 0.8$, second column), the torus is pinched and the SP becomes hyperbolic, but the classical motion remains regular. Increasing the interaction strength further, a stochastic layer appears ($u = 1.1$, third column) and expands until the last KAM torus is destroyed and global chaos is attained ($u = 3.0$, fourth column). Self-trapping then restores integrability in the strong interaction limit ($u = 3.5$, right column). The various transitions are reflected in the measures of Fig. 5 and in the shape of the Husimi distribution function of the SP-supported state.

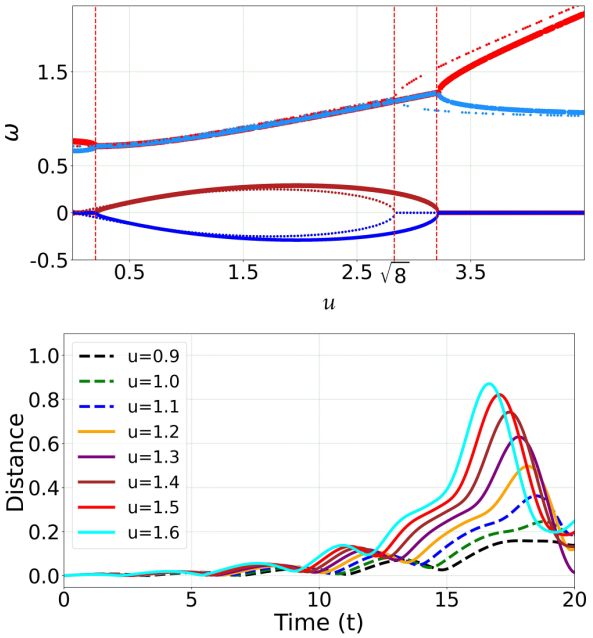

FIG. 4. Stability analysis of the SP. Upper panel: Upper (lower) lines are the real (imaginary) part of the Bogoliubov frequencies, plotted against u. Dotted thin lines and thick solid lines are for detuning $v = 0, 0.1$, respectively. Dynamical instability is indicated by the nonvanishing imaginary component of the frequencies in the range indicated by vertical dotted lines. Lower panel: Distance from the SP as a function of time for an individual trajectory launched very close to the SP. The dependence on u is illustrated and reflects the instability.

The M_2 measure in Fig. 5 does not provide a sharp signature for the transitions. The SP-supported state remains localized even in regimes where the classical dynamics in the vicinity of the SP is extremely unstable. This is further illustrated by indicating the localization region on top of the classical trajectories in the two bottom rows of Fig. 6. The conclusion is that the SP serves as a *pinning center* for the localization of those states, irrespective of whether it is stable or not.

Going back to Fig. 1, we mark with horizontal lines the interaction strength values $u = 0.2, 1.1, 3.2$ that indicate, respectively, the bifurcation of the central SP, the emergence of chaos near the SP, and the transition back to stability.

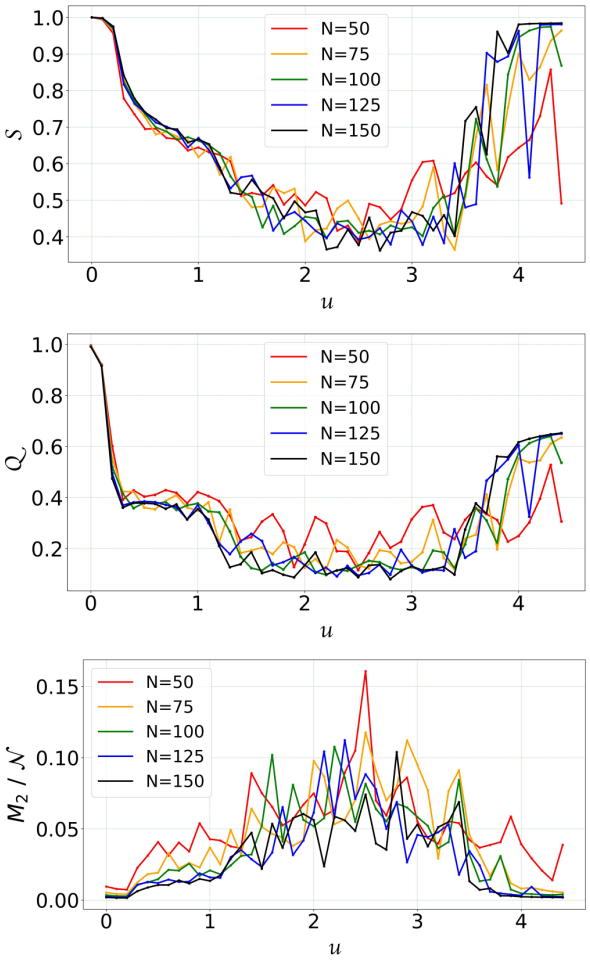

FIG. 5. Characterization of the SP-supported state. The purity S (top), the overlap with the dark state Q (middle), and the participation ratio $M_2/\mathcal{N}$ (bottom) of the SP-supported state are plotted versus the interaction strength u for different values of the total particle number N.

VI. CLASSIFICATION OF MANY-BODY EIGENSTATES

The standard classification of quantum eigenstates includes regular eigenstates supported by quasi-integrable islands in phase space and irregular eigenstates supported by chaos. This classification is already challenged by the fact that the SP-supported states are extremely localized despite being embedded in chaos. However, our analysis below goes further and reveals substantially richer structures. Specifically, while chaotic states may display the well-known random-wave [3] or scarred phase-space distribution, they may also exhibit hybrid localization that is implied by the slow underlying mixed-chaos dynamics. We note that our model has two degrees of freedom, hence Arnold diffusion [30,31] is excluded and any quantum hybridization of chaotic and integrable regions takes place across classically forbidden boundaries.

To demonstrate the above statement, we contrast two regimes of the classical dynamics. For $u = 3.0$, the $E_{\rm SP}$ energy shell is globally chaotic. Nevertheless, the $E > E_{\rm SP}$ range, as opposed to the $E < E_{\rm SP}$ range, features a mixed classical phase space that contains a large integrable island. This is illustrated in Fig. 7, where we plot Poincare sections at representative energies. The tiny island that appears for $E < E_{\rm SP}$ cannot be resolved quantum mechanically, as opposed to the relatively large island that dominates in the $E > E_{\rm SP}$ range. This observation will be further discussed and established below.

The Percival paradigm suggests that the existence of a large island will split the quantum many-body spectrum into regular and irregular groups of eigenstates. Contrary to that, we argue that *hybridized states* are more prevalent. These states have unique statistical properties that distinguish them from regular or fully chaotic eigenstates, and they are responsible for the large spread in M_q values observed in Fig. 3. Their dominance is reflected in the intensity statistics discussed in the following section.

The Husimi phase-space distribution of four representative quantum eigenstates is shown in Fig. 8. The top panels are obtained for parameters where the underlying classical dynamics is globally chaotic throughout the pertinent energy surfaces. While some eigenstates in this regime are a delocalized irregular eigenstate as the one shown in Fig. 8(a), there are also highly localized SP-supported eigenstates like in Fig. 8(b). The bottom panels contrast a chaotic eigenstate [Fig. 8(c)] and an island eigenstate [Fig. 8(d)] lying on the same classically mixed energy surface. As seen below, the distinction between the two is blurred and most eigenstates on this surface lie in between these extreme examples and display hybridization between chaotic and integrable regions.

In the mixed chaos regime, we construct measures that distinguish between chaotic and regular states. Classically, each trajectory is either regular or irregular. The time average of n_2 for all irregular trajectories (blue points in Fig. 9) is the same and equals its mean over the chaotic sea. Doing the same for regular trajectories gives different values associated with the mean over the pertinent invariant tori (red points in Fig. 9). This procedure thus generates a classical skeleton for the many-body spectrum.

Identifying the regular trajectories associated with the red points, we select a subset of coherent states that are located at their Poincare sections (the intersection of the pertinent torus with the $p_1 = 1/2$ plane). The projection Q of the many-body eigenstates onto this subset quantifies their regularity. The results are displayed in the scatter diagram of Fig. 10 where the quantum eigenstates are classified according to their M_2 and Q values. The states presented in Figs. 8(c) and 8(d) are, respectively, one that has a very large value of M_2 (with low Q) and one that has the maximal Q (with low M_2). As such, they are distinctly irregular (chaotic) and regular (island) examples. However, the scatter of the points in Fig. 10 suggests that such binary classification is inappropriate, and that typically the many-body eigenstates cannot be associated with one or another classical region.

VII. INTENSITY STATISTICS

Having identified different families of many-body eigenstates, we now turn to the detailed analysis and

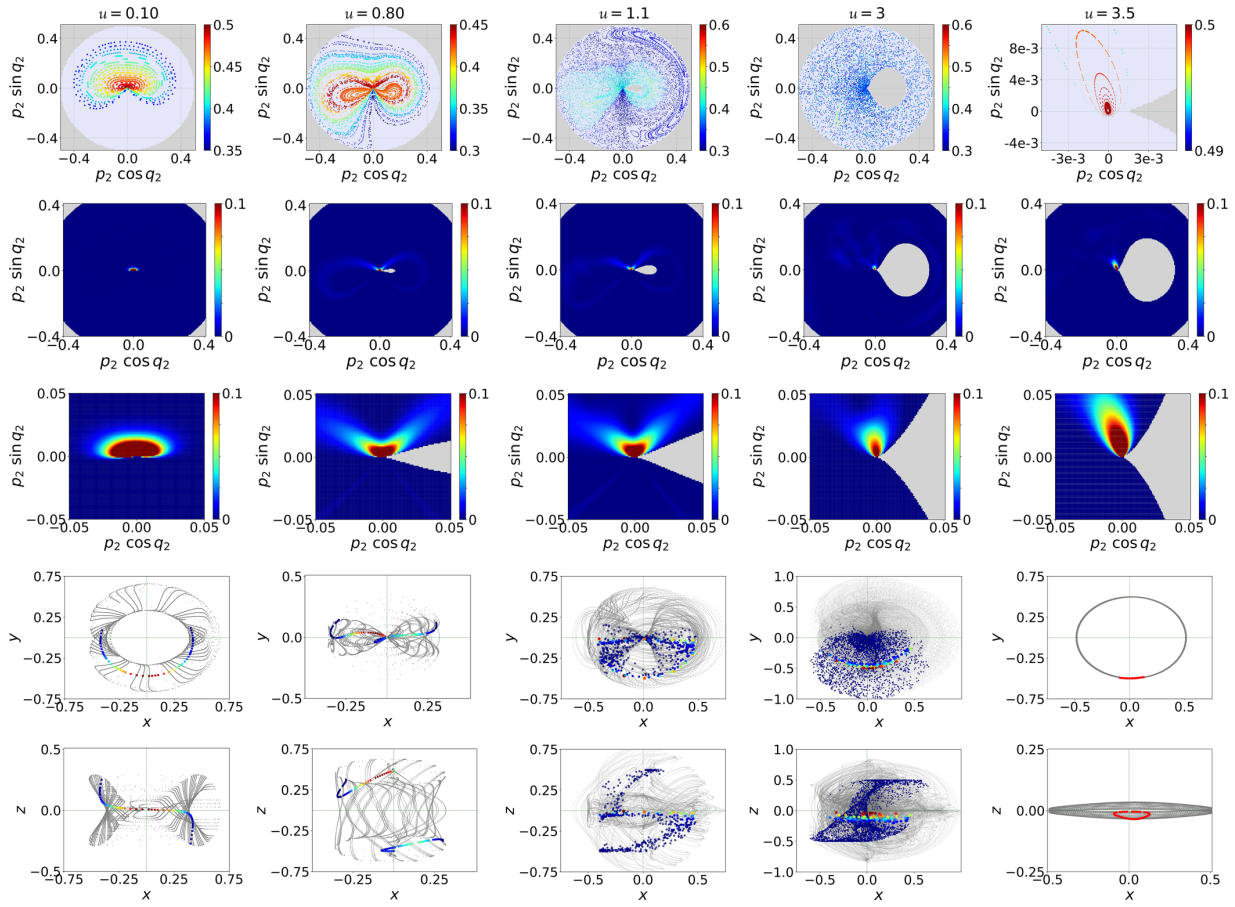

FIG. 6. Classical dynamics vs quantum phase-space distribution of the SP-supported eigenstate. Top row: Poincare sections at $p_1 = 1/2$, taken at $E_{\rm SP}$, namely, along the dashed line of Fig. 1. Five representative values of u were selected, where the SP is stable; unstable but regular; unstable in chaos; embedded in global chaos; and restabilized by self-trapping. The color code represents the average value of p_1 along the trajectory. Second row: The Husimi phasespace distribution of the SP-supported eigenstate for the same values of u. The color code represents the values $|\langle\alpha|E_\nu\rangle|^2$, where ν corresponds to the SP-supported eigenstate index, and the number of particles is $N = 150$. Other parameters are the same as in the previous figures. Third row: Zoom on the same Husimi distributions. Last two rows: 3D plot of representative trajectory for each u from two different view aspects. Points of the Poincare sections are color-coded as in the Husimi plots. The torodial coordinates are $x = (p_2 + p_1 \cos q_1)\cos q_2$, $y = (p_2 + p_1 \cos q_1)\sin q_2$, and $z = p_1 \sin q_1$.

characterization of their Fock-basis intensity distribution, namely, the distribution of the $X_{\nu,n}$, as defined in Eq. (7). The ratio between the different M_q moments of this distribution are set either by its overall envelope or by the statistical noise within it. In the numerical results below, we focus on the particular ratio M_{10}/M_2.

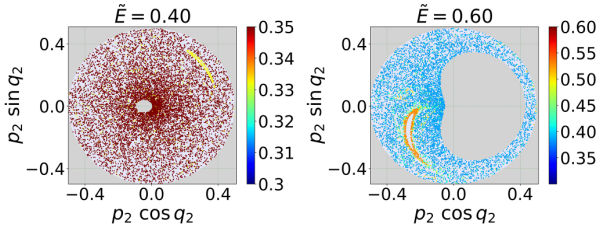

FIG. 7. Hard chaos vs mixed chaos. The $p_1 = 1/2$ Poincare sections are taken in the chaotic interaction regime at energies (a) below and (b) above the stationary point's energy $E_{\rm SP}$. Color code is the average value of p_1 over a given trajectory.

If the variation of $X_{\nu,n}$ as a function of n follows a smooth envelope, the M_q ratios are determined by the line shape. For a uniform distribution $X_{\nu,n} = 1/\mathcal{N}$, we have $M_q = \mathcal{N}$ for all q. By contrast, a power-law line shape results in a rapid drop of M_q as q is increases, leading to very low nonuniversal M_{10}/M_2 ratio.

On the other extreme, the ratio between different M_q can be affected by statistical fluctuations within an otherwise uniform envelope, as in the case of a Billiard system [25]. The GOE statistics typical to fully irregular states in the presence of time-reversal symmetry, yield a universal ratio $M_{10}/M_2 \approx 0.3$. For the hybridized eigenstates that dominate the trimer spectrum, the challenge is to identify what feature of their intensity distribution is responsible for the numerically observed value of M_{10}/M_2.

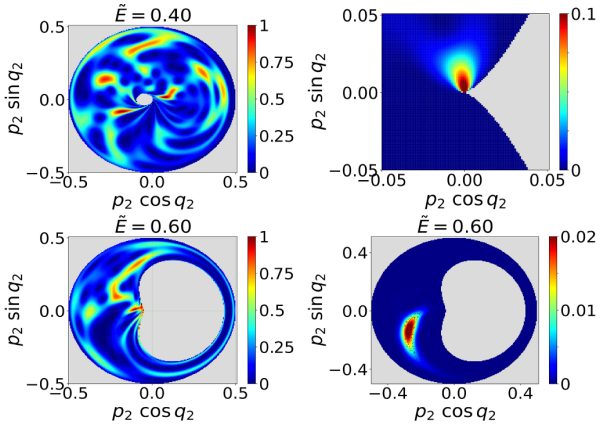

FIG. 8. Husimi functions for representative states. (a) Representative chaotic state in the hard chaos regime $\tilde{E} \sim 0.4$. (b) The SP-supported eigenstate (zoomed). (c) Representative chaotic state in the mixed-chaos regime $\tilde{E} \sim 0.6$. (d) An island state at the same energy. Color codes in (a) and (c) are rescaled with maximum overlap $|\langle\alpha|E_\nu\rangle|^2$ in the panels, while in (b) and (d) color code represents $|\langle\alpha|E_\nu\rangle|^2$.

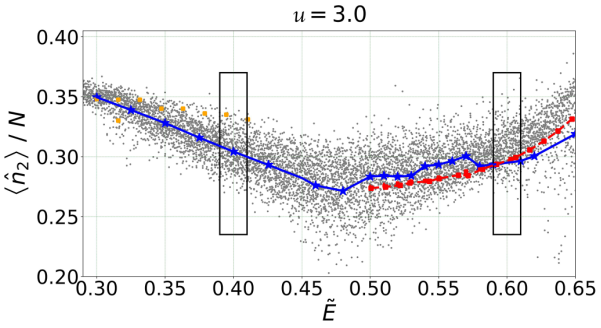

FIG. 9. The classical skeleton of the spectrum. The blue solid line marks the time-averaged value of n_2 for chaotic trajectories. The red dashed line is the time-averaged value of n_2 for regular trajectories corresponding to island states. Rectangles mark the energy windows in which all the states have been considered for scaling and comparison analysis of chaotic states of two kinds, namely, hard chaotic and mixed chaotic.

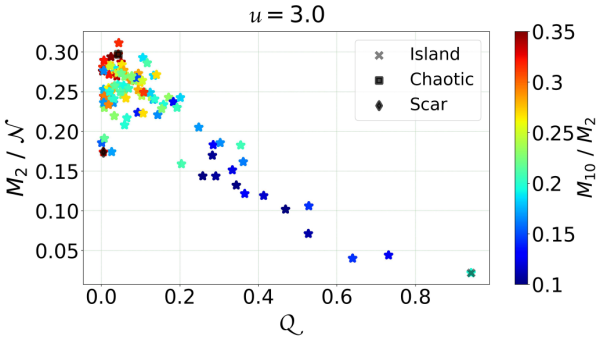

FIG. 10. Hybridization of chaotic and island states. M_2 vs Q, color-coded with M_{10}/M_2. Here Q is the sum of the overlaps (normalized) between the coherent states on the island and energy eigenstates within the energy shell $\tilde{E} = 0.60$.

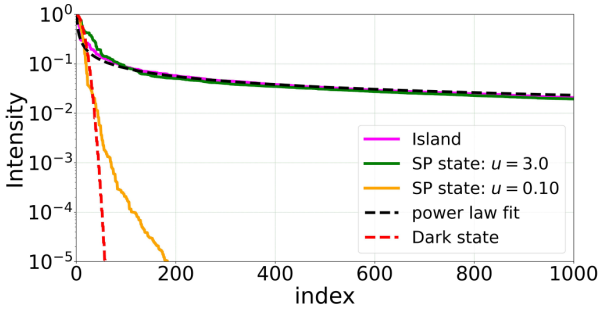

FIG. 11. Line-shape analysis. The sorted values of $X_{\nu,n}$ normalized as intensity $=X_{\nu,n}/\max(X_{\nu,n})$, for the selected island and SP-supported states of Fig. 8. For reference, we show the line shape of a coherent dark state. The dashed curve is $\sim 1/\mathbf{n}^{0.55}$. Vanishingly small intensities that correspond to forbidden regions have been excluded.

The values of $X_{\nu,n}$, sorted according to their size from the largest to the smallest, are plotted in Fig. 11 for the island and SP-supported states. The curves of these eigenstates simply reflect the line shape of their smooth envelope. In the stable regime ($u = 0.1$), the SP-supported eigenstates have an envelope that is similar to a reference coherent dark state. As the interaction strength is increased, stability is lost and chaos emerges ($u = 3$); the SP-supported eigenstates develop long power-law decaying tails, identical to those of the regular island-supported state. We conclude that both the island and the SP-supported eigenstates are pinned down by their classical (island and fixed-point, respectively) localization centers: The tails that extend into the mixed chaotic region reflect power-law localization.

The same procedure is used for chaotic states. In this case, the ordering does not reflect an overall line shape but merely the characteristics of the statistical noise within a rather uniform envelope. Swapping the axes, we obtain a count of the number of intensities that satisfy $X_{\nu,n} > X$ or upon normalization by $\mathcal{N}$ the inverse cumulative histogram $\text{Prob}(X_{\nu,n} > X)$. The latter is displayed in Fig. 12. Chaotic GOE states are

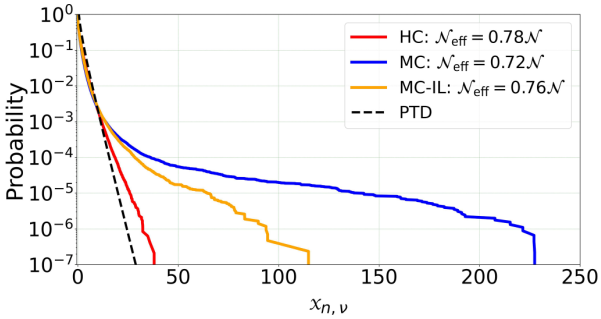

FIG. 12. Intensity statistics for chaotic states. Comparison of Porter-Thomas distribution (PTD) with the intensity distributions of the three different kinds of chaotic groups, namely, hard chaotic (HC), mixed chaotic (MC), and mixed chaotic with island region excluded (MC-IL). Probability on the y axis implies the same as $P(x)$ in Eq. (12).

characterized by the Porter-Thomas statistics Eq. (12). The inverse cumulative histogram of the trimer's eigenstates in the hard chaos regime follows roughly the Porter-Thomas exponential decay with a deviation that may be attributed to an envelope effect that has not been eliminated. By contrast, the inverse cumulative histograms of the eigenstates in the mixed chaos regime have much longer tails. To rule out the possibility that these tails are due to regular states localized in the relatively large island, we eliminate the island from the statistics and obtain a distribution that still deviates substantially from the Porter-Thomas form. We conjecture that there is a hierarchy of smaller and smaller islands that affect the statistics. Thus, the tails of the distribution reflect the non-uniformity of the mixed landscape.

The different classes of many-body eigenstates discussed above have fundamentally different dependence on the effective Planck constant $\hbar \propto 1/N$. In Fig. 13, we plot the dependence of the participation number M_2 and of the ratio M_{10}/M_2 on the total number of particles N. The participation number of the ergodic eigenstates in the hard chaos regime scales as the Hilbert space dimension of the 2 DoF system $M_2 \propto \mathcal{N} \sim N^2$, while the M_{10}/M_2 ratio approaches the expected GOE value $M_{10}/M_2 = 3/9.54 = 0.314$ as N is increased. In contrast, in the mixed chaos regime, the participation number M_2 scales as $N^{1.85}$, while the ratio M_{10}/M_2 drops below the GOE expectation, indicating hybrid localization.

Both island states and SP-supported states that are immersed in chaos exhibit $M_{10}/M_2 \approx 0.22$. This finding supports the claim that the underlying island or the SP are merely pinning centers for a hybrid localized state. The dependence of M_2 on N in both cases is erratic if we follow an individual state that is selected by a maximum overlap criterion. However, for island states, we can accumulate statistics and consider the dependence of the *mean* participation on particle number, obtaining $\bar{M}_2 \propto [\sqrt{N}]^2$ as expected for a minimal wave packet in two-degree of system system. This dependence should be contrasted with the quasi-one-degree-of-freedom result observed for an SP-supported state in the regular region, namely, $M_2 \propto \sqrt{N}$, same as for a dark state. In the latter case, $M_{10}/M_2 \approx 0.8$ as expected.

Our findings are summarized in Table I where the obtained dependence of M_2 on N and the ratio M_{10}/M_2 for the different classes of many-body eigenstates are compared to the expected behavior of states that possess various line shapes and statistical fluctuations.

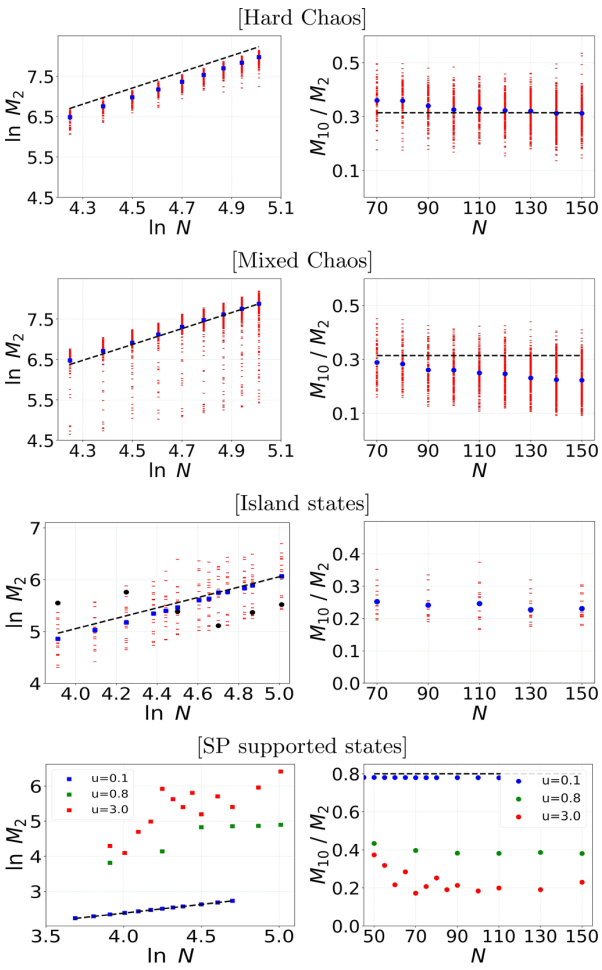

FIG. 13. The N dependence of the statistics. (a) Scaling of the states in the hard chaos regime (left), with the slope = 1.94. (b) Scaling of the states in the mixed chaos regime (right), with the slope = 1.85. (c) Scaling of the island state with the slope = 1. Black dots in the $\ln M_2$ vs $\ln N$ plot are the M_2 values of a single eigenstate in the energy shell $\tilde{E} = 0.60$ and fluctuates with N. (d) Scaling of the SP-supported state with the slope = 1/2. Slope in all the figures refers to the slope of the curve $\ln M_2$ vs $\ln N$.

VIII. SUMMARY

Considering a generic many-body Hamiltonian system that features a mixed classical phase space with chaotic and quasiregular motion, one can identify in the spectrum irregular and regular eigenstates. However, these are idealizations and most quantum eigenstates do not adhere to the traditional paradigm. In this paper, we have highlighted two notable deviations from the binary regular-irregular classification: strongly localized eigenstates in a fully chaotic classical phase space and hybrid eigenstates that extend across chaos-integrability borders in a mixed phase space.

In the first case, eigenstates remain localized in regions where the classical chaotic dynamics is slow with respect to some characteristic quantum timescale (e.g., the Heisenberg time). This type of localization, known as dynamical localization, is related to the theory of Anderson localization in disordered systems [32–34]. Slow regions in phase space are found near the boundaries of the chaotic sea, as discussed in Ref. [17], or in the vicinity of unstable stationary points, as illustrated in this paper.

The majority of the eigenstates in mixed phase space regions are hybrid. They are pinned by the underlying rugged phase-space structure. Past literature has emphasized localization due to the last KAM torus that is destroyed in the Chirikov scenario or due to the remnants of the last KAM torus, aka cantori, or by remnants of unstable manifolds [18–20]. Such

TABLE I. Characterization of quantum states. Summary of the expected M_{10}/M_2 ratio and the power-law dependence of the participation number M_2 on N for several reference states (top block) and various classes of trimer eigenstates (bottom block).

Standard states		
State type	M_{10}/M_2	Slope
Dark state $\alpha = \frac{1}{\sqrt{2}}(1, 0, -1)$	0.80	1/2
Generic coherent state	0.65	1
Rectangular: $X_n = 1/\mathcal{N}$	1	2
GOE: $X_n \sim 1/\mathcal{N}$+fluctuations	0.3145	2
Power law: $X_n \propto 1/n^{0.5}$	∼0.22	∼0.45
SP state (stable)	∼0.78	1/2
SP state (unstable regular)	∼0.4	noisy
SP state (unstable chaotic)	∼0.22	noisy
Island state: $u = 3.0$	∼0.22	1
Mixed chaos: $u = 3.0$	∼0.22	1.85
Hard chaos: $u = 3.0$	∼0.313	∼1.94

localization mechanisms are highly specific and occur only if the model parameters are carefully tuned. A related scenario can be seen in Fig. 6 for $u = 1.1$, where the last KAM still survives, but it does not signify a dramatic crossover in the global statistics.

Contrasting with previous publications, we realize here that the signature of the mixed phase space persists for a wide range of u values. On the practical side, we have utilized M_q ratios as a measure for the identification of families of states that do not fall under standard categorization. Such generalized entropy measures should be employed in the spectral analysis of any system with a mixed phase space.

The effects of scarring, localization, and hybridization are all related to the underlying classical phase space, and it might be useful to summarize what classical ingredients are required for the analysis. It is possibly natural to start with Lyapunov exponent analysis as in Ref. [8]. Local dispersion in the value of the largest exponent may indicate mixed regions of regular and chaotic motion, as opposed to ergodic regions where it has a well-defined value. In a fully chaotic region, an idealized theory [12] provides a direct relation between the scar intensity and the instability exponents of the underlying periodic orbits. Stationary points at the *corners* of phase space are somewhat special and possibly can be regraded as the upper unstable fixed-point of a mathematical pendulum. More generally, near the boundaries that separate chaotic from quasiregular regions, the distribution of the Lyapunov exponents becomes fragmented, and dynamical localization is related to the transport coefficients of the slow dynamics. The latter are not determined merely by the Lyapunov spectrum, and in some cases are related to cantori or to remnants of unstable manifolds [18–20]. Irrespective of the localization mechanism, dynamical tunneling allows hybridization that blurs the classification of eigenstates.

ACKNOWLEDGMENT

This research was supported by the Israel Science Foundation (Grant No. 518/22). We thank Maxim Olshanii for valuable discussions.

APPENDIX: STABILITY ANALYSIS FOR THE CENTRAL SP

The classical SPs of the Bose-Hubbard trimer model are found by solving

$$i\dot{\mathbf{a}} = (H_0 + u\mathcal{P})\boldsymbol{a} = \mu\boldsymbol{a}, \tag{A1}$$

where $\boldsymbol{a} = (1/\sqrt{N})(a_1, a_2, a_3)$ represents rescaled classical amplitudes and the operators H_0 and $\mathcal{P}$ are

$$H_0 = \begin{pmatrix} 0 & -\frac{\Omega}{2} & 0 \\ -\frac{\Omega}{2} & v & -\frac{\Omega}{2} \\ 0 & -\frac{\Omega}{2} & 0 \end{pmatrix}, \quad \mathcal{P} = \begin{pmatrix} P_1 & 0 & 0 \\ 0 & P_2 & 0 \\ 0 & 0 & P_3 \end{pmatrix}, \tag{A2}$$

where $P_i = |a_i|^2/N$. The dark-state SP is given by $\boldsymbol{a} = \alpha_{\rm SP} = (1/\sqrt{2}, 0, -1/\sqrt{2})$. The dynamical stability analysis of this SP is carried out via diagonalization of the Bogoliubov matrix,

$$\begin{pmatrix} H_0 + 2u\mathcal{P} - \mu & -u\mathcal{P} \\ u\mathcal{P} & -(H_0 + 2u\mathcal{P} - \mu) \end{pmatrix}, \tag{A3}$$

resulting in three pairs of characteristic frequencies, namely, $\pm\omega_q$ indexed by $q = \{0, +, -\}$. The trivial frequency $\omega_0 = 0$ is implied by conservation of particles, while

$$\omega_+ = \frac{\sqrt{\sqrt{((u-2v)^2+4)^2 - 16(u^2-2uv+1)} + u^2 - 4uv + 4v^2 + 4}}{2\sqrt{2}},$$

$$\omega_- = \frac{\sqrt{-\sqrt{(u-2v)(u^3-6u^2v+4u(3v^2-2)-8v(v^2+2))} + (u-2v)^2 + 4}}{2\sqrt{2}}.$$

For $v = 0$, the nonvanishing frequencies coalesce to give

$$\omega_\pm = \pm\frac{1}{2\sqrt{2}}[(4 + u^2) \pm u\sqrt{u^2 - 8}]^{1/2}. \tag{A4}$$

[1] I. C. Percival, Regular and irregular spectra, J. Phys. B **6**, L229 (1973).
[2] E. B. Stechel and E. J. Heller, Quantum ergodicity and spectral chaos, Annu. Rev. Phys. Chem. **35**, 563 (1984).
[3] M. V. Berry, Regular and irregular semiclassical wavefunctions, J. Phys. A: Math. Gen. **10**, 2083 (1977).
[4] M. Srednicki, Chaos and quantum thermalization, Phys. Rev. E **50**, 888 (1994).
[5] L. D'Alessio, Y. Kafri, A. Polkovnikov, and M. Rigol, From quantum chaos and eigenstate thermalization to statistical mechanics and thermodynamics, Adv. Phys. **65**, 239 (2016).
[6] J. M. Deutsch, Eigenstate thermalization hypothesis, Rep. Prog. Phys. **81**, 082001 (2018).
[7] R. Nandkishore and D. A. Huse, Many-body localization and thermalization in quantum statistical mechanics, Annu. Rev. Condens. Matter Phys. **6**, 15 (2015).
[8] G. Nakerst and M. Haque, Chaos in the three-site Bose-Hubbard model: Classical versus quantum, Phys. Rev. E **107**, 024210 (2023).
[9] E. J. Heller, Quantum localization and the rate of exploration of phase space, Phys. Rev. A **35**, 1360 (1987).

[10] S. Fishman, D. R. Grempel, and R. E. Prange, Chaos, quantum recurrences, and Anderson localization, Phys. Rev. Lett. **49**, 509 (1982).

[11] G. Casati and J. Ford, *Stochastic Behavior in Classical and Quantum Hamiltonian Systems: Volta Memorial Conference, Como 1977* (Springer, Berlin, Heidelberg, 1979).

[12] L. Kaplan, Scars in quantum chaotic wavefunctions, Nonlinearity **12**, R1 (1999).

[13] C. J. Turner, A. A. Michailidis, D. A. Abanin, M. Serbyn, and Z. Papić, Weak ergodicity breaking from quantum many-body scars, Nat. Phys. **14**, 745 (2018).

[14] S. Sinha and S. Sinha, Chaos and quantum scars in Bose-Josephson junction coupled to a bosonic mode, Phys. Rev. Lett. **125**, 134101 (2020).

[15] M. Serbyn, D. A. Abanin, and Z. Papić, Quantum many-body scars and weak breaking of ergodicity, Nat. Phys. **17**, 675 (2021).

[16] C. Khripkov, A. Vardi, and D. Cohen, Semiclassical theory of strong localization for quantum thermalization, Phys. Rev. E **97**, 022127 (2018).

[17] C. Khripkov, A. Vardi, and D. Cohen, Many-body dynamical localization and thermalization, Phys. Rev. A **101**, 043603 (2020).

[18] N. T. Maitra and E. J. Heller, Quantum transport through cantori, Phys. Rev. E **61**, 3620 (2000).

[19] M. Firmbach, A. Backer, and R. Ketzmerick, Partial barriers to chaotic transport in 4D symplectic maps, Chaos **33**, 013125 (2023).

[20] J. Stöber, A. Bäcker, and R. Ketzmerick, Quantum transport through partial barriers in higher-dimensional systems, Phys. Rev. Lett. **132**, 047201 (2024).

[21] O. Dutta, M. Gajda, P. Hauke, M. Lewenstein, D.-S. Luhmann, B. A. Malomed, T. Sowiski, and J. Zakrzewski, Non-standard Hubbard models in optical lattices: A review, Rep. Prog. Phys. **78**, 066001 (2015).

[22] G. Arwas, A. Vardi, and D. Cohen, Superfluidity and chaos in low dimensional circuits, Sci. Rep. **5**, 13433 (2015).

[23] A. Richaud and V. Penna, Phase separation can be stronger than chaos, New J. Phys. **20**, 105008 (2018).

[24] C. E. Porter and R. G. Thomas, Fluctuations of nuclear reaction widths, Phys. Rev. **104**, 483 (1956).

[25] H. Alt, H. D. Gräf, H. L. Harney, R. Hofferbert, H. Lengeler, A. Richter, P. Schardt, and H. A. Weidenmüller, Gaussian orthogonal ensemble statistics in a microwave stadium billiard with chaotic dynamics: Porter-thomas distribution and algebraic decay of time correlations, Phys. Rev. Lett. **74**, 62 (1995).

[26] E. M. Graefe, H. J. Korsch, and D. Witthaut, Mean-field dynamics of a Bose-Einstein condensate in a time-dependent triple-well trap: Nonlinear eigenstates, Landau-Zener models, and stimulated Raman adiabatic passage, Phys. Rev. A **73**, 013617 (2006).

[27] C. J. Pethick and H. Smith, Dynamics of the condensate, in *Bose-Einstein Condensation in Dilute Gases* (Cambridge University Press, Cambridge, 2008), pp. 182–224.

[28] J. Moser, Nearly integrable and integrable systems, AIP Conf. Proc. **46**, 1 (1978).

[29] H. S. Dumas, *The KAM Story* (World Scientific, Singapore, 2014).

[30] D. Basko, Weak chaos in the disordered nonlinear Schrodinger chain: Destruction of Anderson localization by Arnold diffusion, Ann. Phys. **326**, 1577 (2011).

[31] B. V. Chirikov, A universal instability of many-dimensional oscillator systems, Phys. Rep. **52**, 263 (1979).

[32] P. W. Anderson, Absence of diffusion in certain random lattices, Phys. Rev. **109**, 1492 (1958).

[33] F. Evers and A. D. Mirlin, Anderson transitions, Rev. Mod. Phys. **80**, 1355 (2008).

[34] G. Modugno, Anderson localization in Bose-Einstein condensates, Rep. Prog. Phys. **73**, 102401 (2010).